

PAPER

# Thermal graphene metamaterials and epsilon-near-zero high temperature plasmonics

To cite this article: Sarang Pendharker *et al* 2017 *J. Opt.* **19** 055101

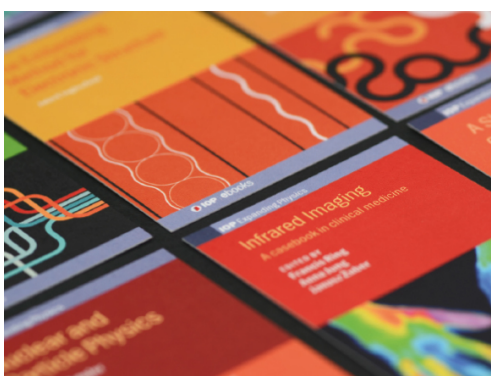
View the [article online](#) for updates and enhancements.

## Related content

- [Roadmap on optical energy conversion](#)  
Svetlana V Boriskina, Martin A Green, Kylie Catchpole *et al*.
- [Wavelength-selective emitters with pyramid nanogratings enhanced by multiple resonance modes](#)  
Nghia Nguyen-Huu, Jaromír Pištora and Michael Cada
- [Roadmap on optical metamaterials](#)  
Augustine M Urbas, Zubin Jacob, Luca Dal Negro *et al*.

## Recent citations

- [Frequency-tunable terahertz angular selectivity based on a dielectric-graphene multilayer structure](#)  
Feng Wu *et al*
- [Scale Law of Far-Field Thermal Radiation from Plasmonic Metasurfaces](#)  
Jiayu Li *et al*
- [Spectral domain inverse design for accelerating nanocomposite metamaterials discovery](#)  
Ashwin K. Boddeti *et al*



**IOP | ebooks™**

Bringing together innovative digital publishing with leading authors from the global scientific community.

Start exploring the collection—download the first chapter of every title for free.

# Thermal graphene metamaterials and epsilon-near-zero high temperature plasmonics

Sarang Pendharker<sup>1</sup>, Huan Hu<sup>1</sup>, Sean Molesky<sup>1</sup>, Ryan Starko-Bowes<sup>1</sup>,  
Zohreh Poursoti<sup>1</sup>, Sandipan Pramanik<sup>1</sup>, Neda Nazemifard<sup>2</sup>,  
Robert Fedosejevs<sup>1</sup>, Thomas Thundat<sup>2</sup> and Zubin Jacob<sup>1,3</sup>

<sup>1</sup> Department of Electrical and Computer Engineering, University of Alberta, Edmonton, AB T6G 2V4, Canada

<sup>2</sup> Department of Chemical and Materials Engineering, University of Alberta, Edmonton, AB T6G 2V4, Canada

<sup>3</sup> Birck Nanotechnology Center, School of Electrical and Computer Engineering, Purdue University, West Lafayette, IN 47906, United States of America

E-mail: [zjacob@ualberta.ca](mailto:zjacob@ualberta.ca)

Received 1 December 2016, revised 1 February 2017

Accepted for publication 13 February 2017

Published 31 March 2017



CrossMark

## Abstract

The key feature of a thermophotovoltaic (TPV) emitter is the enhancement of thermal emission corresponding to energies just above the bandgap of the absorbing photovoltaic cell and simultaneous suppression of thermal emission below the bandgap. We show here that a single layer plasmonic coating can perform this task with high efficiency. Our key design principle involves tuning the epsilon-near-zero frequency (plasma frequency) of the metal acting as a thermal emitter to the electronic bandgap of the semiconducting cell. This approach utilizes the change in the reflectivity of a metal near its plasma frequency (epsilon-near-zero frequency) to lead to spectrally selective thermal emission, and can be adapted to large area coatings using high temperature plasmonic materials. We provide a detailed analysis of the spectral and angular performance of high temperature plasmonic coatings as TPV emitters. We show the potential of such high temperature plasmonic thermal emitter coatings (p-TECs) for narrowband near-field thermal emission. We also show the enhancement of near-surface energy density in graphene-multilayer thermal metamaterials due to a topological transition at an effective epsilon-near-zero frequency. This opens up spectrally selective thermal emission from graphene multilayers in the infrared frequency regime. Our design paves the way for the development of single layer p-TECs and graphene multilayers for spectrally selective radiative heat transfer applications.

Keywords: hyperbolic metamaterials, epsilon-near-zero metamaterials, plasmonics

(Some figures may appear in colour only in the online journal)

## 1. Introduction

Thermophotovoltaic (TPV) systems promise to provide high efficiency energy conversion from heat to electricity by spectrally matching the thermal emission from an emitter to the bandgap of a conventional single-junction photovoltaic cell [1–5]. This field of research has seen a resurgence in

recent years due to parallel developments in the fields of nanoscale thermal engineering [6], nanofabrication [7, 8] and high temperature material science [9–12]. An important aspect of the TPV system is the design of the emitter, which has to suppress the thermal emission of sub-bandgap photons as they cannot be converted to electrical output [7, 8], and simultaneously enhance thermal emission just above the cell

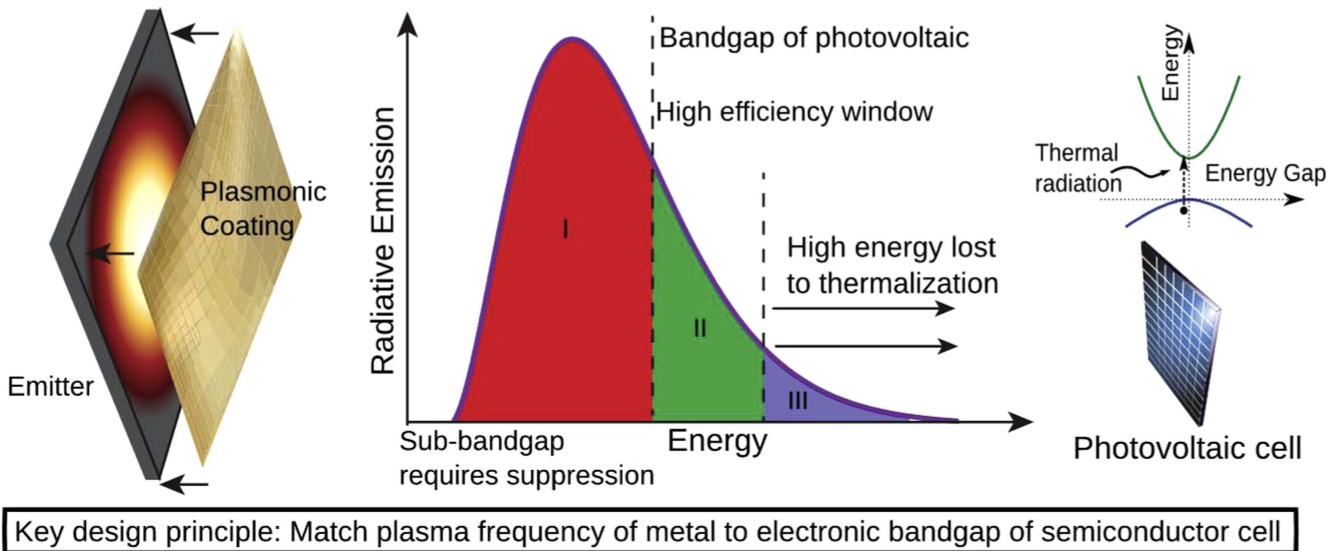


**Figure 1.** Efficient TPV energy conversion requires two critical features: (1) Suppression of thermal radiation with energy less than the band-gap of the PV cell. (2) Enhancement of thermal radiation within the high efficiency window of energies which lie directly above the PV cell band-gap. Both of these goals can be accomplished by tuning the plasma frequency (epsilon-near-zero frequency) of a high temperature plasmonic thermal emitter coating (p-TEC).

bandgap. Note that sub-bandgap blackbody photons are the primary reason for the decrease in the efficiency of energy conversion (see figure 1). One necessary requirement for an emitter is a robust optical response and thermal/structural stability of the emitter which has to withstand high temperatures [1].

Significant recent advances have shown the potential of photonic crystals [7, 8, 12–15], thin films [3, 11, 16–24], perfect absorbers [24], thermal metamaterials [10, 25–28], tungsten metasurfaces [28–30], graphene [31, 32], surface waves [33, 34] and other nanophotonic structures [2, 35] to engineer the thermal emission [36, 37] and achieve spectrally selective emitters [36–38]. Simultaneously, work has progressed to advance the critical challenge involving the absorber/TPV cell design.

Molesky *et al* introduced the concept of high temperature plasmonics and metamaterials [10]. Here, we build on our previous work regarding the initial suggestion of high temperature plasmonics [10, 11] and experimental demonstration of high temperature thermal metamaterials [25]. In this paper, we provide an alternative in selective emitter design employing only a single layer of plasmonic thermal emitter coating (p-TEC). This design holds the significant advantage of not requiring 2D patterning to achieve the desired optical response. Along with the ease of large area fabrication, it also opens up the possibility of high temperature stable operation since 2D texturing often reduces the melting point of metals. The primary objective of the thermal suppression of sub-bandgap photons can be achieved by tuning the epsilon-near-zero (ENZ) frequency (also known as plasma frequency) of a metal to the bandgap of the cell. Thus natural material properties provide the reflectivity change desired for the thermal emitter as opposed to structural bandgap effects as in photonic crystals. We also show that our design is useful for

engineering narrowband near-field thermal emission, paving the way for a unified platform for both far-field and near-field thermal emitters. We also provide a detailed performance analysis for our thin film designs. It should be noted that polar dielectric thin films (e.g. silicon carbide) only show phonon-polaritonic resonances and an ENZ regime only in the mid-infrared frequency ranges and not in the near-infrared range conducive for high temperature TPV applications.

One important application of selective thermal emitters is the ability to modulate thermal emission along with a spectrally selective nature [39–42]. Graphene presents an ideal platform to achieve this effect due to the strong electrical tunability of its optical absorption properties [43]. Graphene is expected to find wide applications in next generation electronic devices due to its good electrical [44] and thermal properties [45] and strong light–matter interactions [46]. A substrate coated with a graphene layer has been reported to have highly directive far-field thermal emission, enhanced light absorption [47] and enhanced near-field radiation transfer [48, 49]. An important emerging platform is that of multilayer graphene based metamaterials [50–52], which have been reported to exhibit tunable absorption and hyperbolic dispersion [53–55].

In this paper, we report a sharp suppression in the thermal emissivity of a graphene-multilayer structure, and show that it can be controlled by tuning the topological transition in the graphene metamaterial. We also report a sharp enhancement in the near-field thermal emission in graphene-multilayers due to topological transitions. These results form a crucial step in the realization of thermal energy scavenging technologies in future graphene-based electronic devices. We note that the opportunity to electrically tune topological transitions can be an important design principle for spectrally selective thermal modulation.

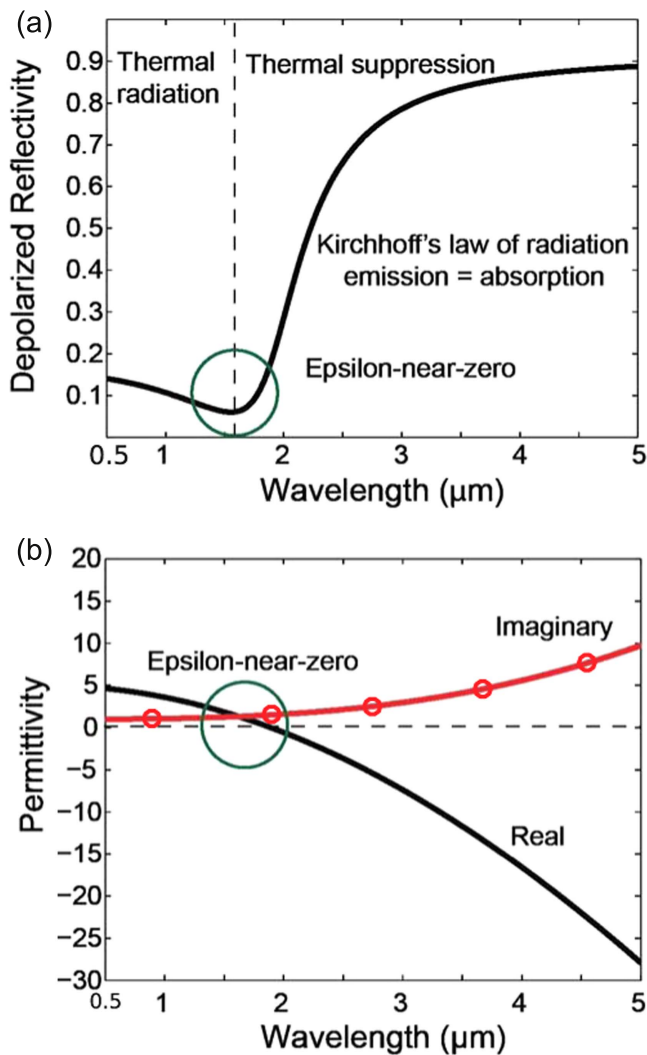


**Figure 2.** (a) Depolarized (averaged  $s$  and  $p$  polarized) normal reflectivity from plasmonic half space. High reflectivity beyond the epsilon-near-zero (ENZ) wavelength implies a low absorptivity/emissivity (thermal suppression of low energy sub-bandgap photons). Note, Kirchhoff's laws require the far-field emissivity of the plasmonic half space to be its absorptivity. (b) By shifting the plasma frequency (ENZ frequency) of the metal, the spectral content of the emitted radiation can be engineered to match the bandgap of a photovoltaic cell. This arises through the sharp change of the metal's reflectivity at its plasma frequency. The sample Drude metal considered here is assumed to have a background dielectric constant of 5, a plasma frequency of 0.66 eV and a loss parameter of 70 meV.

## 2. High temperature p-TEC

Selective thermal emitters for TPVs have to perform the important function of thermal suppression below the bandgap of the absorbing cell and simultaneously enhance emission just above the PV cell bandgap [13, 56]. We design this feature by employing a thin film of Drude metal with engineered plasma frequency (ENZ frequency) and no surface patterning. The plasma frequency is the characteristic frequency above which metals lose their reflectivity and become transparent. Thus metals absorb above the plasma frequency and reflect light below the plasma frequency. Figures 2(a) and (b) show the correspondence between a sharp reflectivity

change at normal incidence and the ENZ wavelength for a Drude metal. The high reflectivity leads to decreased optical absorption and suppresses the thermal emission by Kirchhoff's law (absorptivity = emissivity). One can therefore achieve the suppression of sub-bandgap thermal emission simply by tuning the plasma frequency in the near-infrared range close to the bandgap of the TPV cell. The design achieves enhancement in thermal emission in the transparency range of the metal tuned to be above the bandgap of the cell. Note, all metals are transparent and lossy above the ENZ frequency (plasma frequency), giving rise to large absorption and emission.

## 3. High temperature material properties

We now outline the choices for high temperature metals that can act as a plasmonic thermal emitter coating. Even though tungsten and tantalum have excellent thermal properties [56], the plasma frequency (ENZ frequency) cannot be tuned to the near-infrared range to match the low energy bandgap of gallium antimonide or germanium TPV cells. We have performed a detailed analysis of titanium nitride and zirconium nitride, which are refractory metals with a plasmonic response for TPV applications [9, 57]. Our analysis (to be published later) indicates that their interband transitions and losses, especially in the near-infrared region, are sub-optimal for both the far-field and the near-field plasmonic thermal emitter performance. They will need to be optimized to find use in TPV systems as a thin film plasmonic coating but can be used as nanoantennas [9, 57]. In this work, we therefore focus on the use of aluminum doped zinc oxide (AZO) and gallium doped zinc oxide (GZO) with a plasma frequency (ENZ frequency) tuned in the near-infrared for p-TECs [58, 59]. In general, the optical response of materials at high temperatures poses a significant challenge for thermal emitter design. We have utilized empirical models of tungsten and AZO/GZO available in the literature to arrive at general conclusions of the real part and imaginary part of the response at high temperatures [58–66]. Increasing temperature causes a rise in electron–phonon interactions and simultaneous reduction of collision time. This is manifested in a reduction of the bulk polarization response and an increase in optical absorption. Consequently, the real part of the dielectric constant governing the polarization response is reduced and the imaginary part of the dielectric constant governing losses is increased. Thus the performance of plasmonic components is expected to be reduced at high temperatures. A detailed analysis of these empirical models will be published later.

## 4. High temperature thermal emission suppression

### 4.1. Far-field thermal emission: thin-film AZO and other approaches

We now provide the results of calculations using an AZO p-TEC. Using Kirchhoff's laws [67], we calculate the

emissivity of an AZO film with a thickness of 600 nm, 1000 nm and 1400 nm placed on a tungsten substrate (figure 3(a)). It can be observed that there is a sharp suppression in the emissivity above the ENZ wavelength of 1400 nm, irrespective of the thickness of the AZO film. This is because the spectral thermal emission response is dominated by the material properties of the AZO, and the thickness only effects the ripples in the high emissivity region. Figure 3(b) shows the emissivity of a 1000 nm thick AZO film at different emission angles. The inset shows the real and imaginary part of the AZO dielectric response. The emissivity performance at different emission angles displays a similar cut-off behavior, which is necessary for TPV applications. The p-TEC (figure 3(b)) achieves an emissivity profile very close to a tungsten photonic crystal (PhC) design (figure 3(c)). However, note that there are fundamental differences in the approach to achieving thermal suppression. The PhC utilizes a structural resonance and interference effects whereas the p-TEC uses an engineered material response. A simple thin-film coating with an engineered material response matches the performance of a microfabricated photonic crystal.

Thin-film p-TEC with an engineered material response also outperforms thin-film anti-reflection coatings. Figure 4 compares the performance of an anti-reflection coating (AR) [68] as a selective thermal emitter. Figure 4(a) shows the spectral irradiance from an AZO coated tungsten substrate at 1700 K. In comparison with black body radiation, it can be clearly seen that the thermal radiation in the sub-bandgap region is suppressed. This sharp suppression at high wavelengths is because the emissivity of the AZO coating drops above the ENZ wavelength. The thickness of the AZO film is 1000 nm. Figure 4(b) shows the thermal radiation from a tungsten substrate coated with TiO<sub>2</sub> AR coating. Enhancement in the thermal emission near 1500 nm wavelength in the AR coating is due to the enhanced absorptivity arising from the Fabry–Perot resonance mode in a TiO<sub>2</sub> film with a thickness of 355 nm. The peak emittance in TiO<sub>2</sub> can therefore be tuned by tuning the thickness of the AR coating. This is in contrast to the AZO thin film, where the suppression in the emissivity is governed by the material response while the thickness has only a minor effect on the emissivity at the transparent low-wavelength region of the spectrum. It can be seen that even at sub-bandgap wavelengths, the thermal emission in TiO<sub>2</sub> is considerably larger as compared to the AZO coating. The incomplete thermal suppression in the AR coating degrades its efficiency performance.

To provide a performance comparison in the limiting ideal case of these various emitter designs for TPV applications, we apply the Schockley–Queisser detailed balance analysis [13]. In performing this calculation we assume the photovoltaic cell in all cases to be a perfectly absorbing, ideal pn-junction, with a bandgap of 2250 nm for the photonic crystal emitter and 1700 nm for the AZO plasmonic coating and titanium dioxide anti-reflection coating designs. We also assume that the emitter and photovoltaic cell have the same flat area, and that no absorbing stage is present. Under these conditions, the conversion efficiency of the radiated thermal energy into electrical energy in AZO, the photonic crystal and

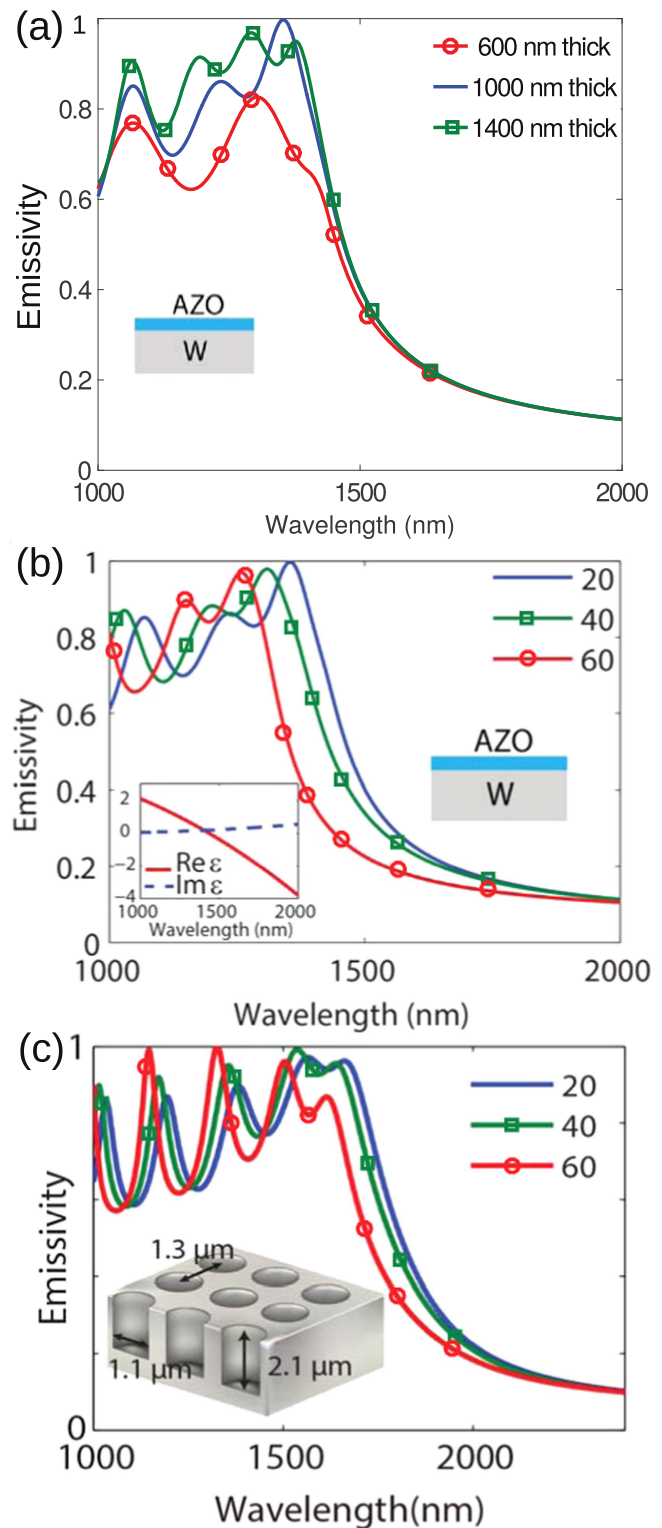


**Figure 3.** A single layer of AZO can suppress the long-wavelength emissivity, similar to a microfabricated tungsten photonic crystal (PhC). (a) Emissivity spectra of AZO thin film on a tungsten substrate at 20° emission angle and varying AZO thickness. (b) Emissivity spectra of 1000 nm AZO film on a tungsten substrate at different emission angles. Inset: real and imaginary part of AZO dielectric permittivity. Beyond 1400 nm the emissivity is suppressed by a large impedance mismatch with vacuum. (c) Emissivity of tungsten PhC at different angles. Inset: schematic of the PhC structure. By controlling the bandgap of photonic crystals, we can tune the emissivity cut-off match wavelength to the PV cell bandgap.

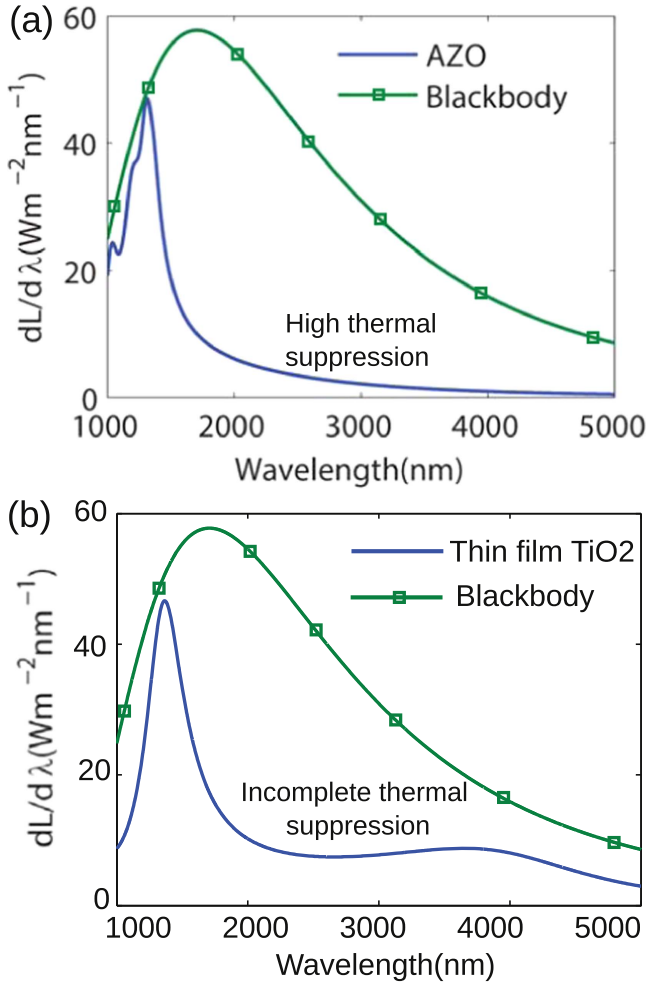


**Figure 4.** AZO thin-film outperforms TiO2 thin-film in the suppression of sub-bandgap thermal emission. (a) Spectral irradiance ( $dL/d\lambda$ ) of an AZO single layer in comparison with a black body at 1700 K (40 degrees emission angle). The selective spectral irradiance shows a large thermal suppression of the sub-bandgap photons and enhanced thermal emission below the ENZ wavelength (above the plasma energy). (b) Spectral irradiance of a single layer TiO2 anti-reflection coating design at 1700 K and 40 degrees emission angle. The enhanced absorption in TiO2 near 1500 nm arises from the Fabry–Perot mode resonance so the peak emittance can be tuned by changing the thickness of the anti-reflection coating. However, the suppression of the sub-bandgap photons is incomplete in the TiO2 layer, resulting in reduced conversion efficiency.

**Table 1.** Comparison of conversion efficiency in AZO, photonic crystal and TiO2 AR coating.

Temperature	AZO thin-film	Photonic crystal	TiO2
1700 K	31.9%	36.7%	19.6%
1300 K	19.4%	29.1%	9.2%

TiO2 coating is shown in table 1. The efficiency of a simple AZO thin-film is less than, but comparable with, the photonic crystal spectrally selective emitter, while it outperforms the TiO2 thin film. The poor efficiency of TiO2 is due to the incomplete thermal suppression at higher wavelengths.

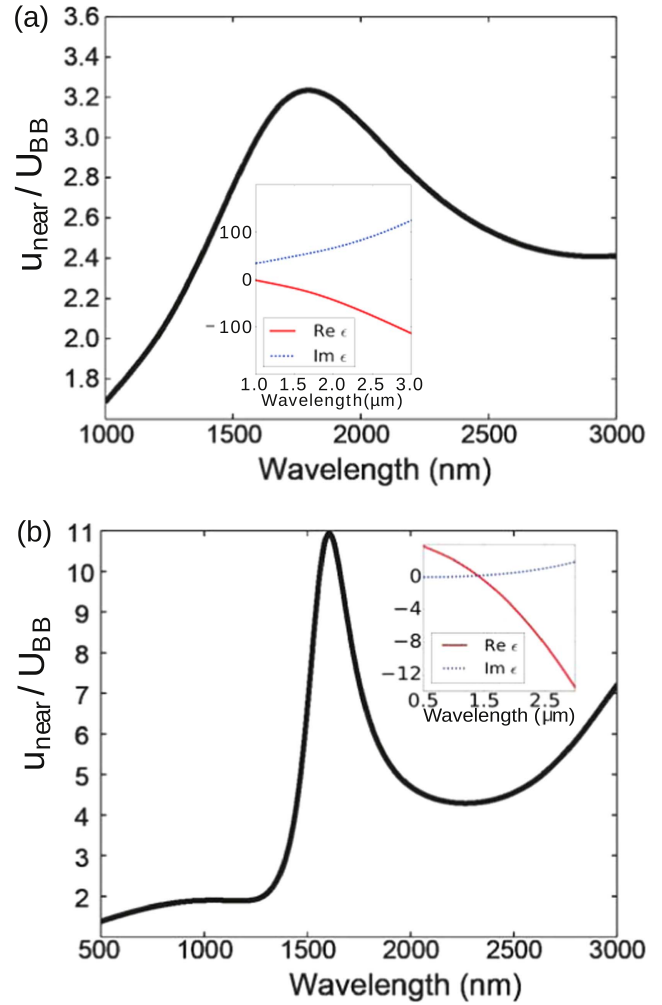


**Figure 5.** Near-field energy density at a distance of 100 nm above (a) a 20 nm tungsten film on a sapphire substrate, and (b) a 55 nm gallium-doped-zinc-oxide film [18] on a boron carbide substrate [22] relative to that of a black body. The p-TEC shows a near-field enhancement by a factor of three over the thin film tungsten. Inset in (a) and (b) shows the permittivity of tungsten and GZO respectively.

#### 4.2. Narrow-band near-field thermal emission

A fundamental advantage of the p-TEC design is that it can simultaneously be used as a near-field emitter and can exhibit narrowband near-field thermal emission. This arises due to thin film surface plasmon polaritons excited at high temperatures, which lead to narrowband thermal emission with potential applications for near-field TPV. While fundamentally challenging to implement, near-field TPVs promise to achieve a high efficiency of conversion with high current densities [69]. This is because near-field thermal energy transfer mediated by evanescent waves can exceed the far-field black body limit.

In figure 5(a), we plot the energy density in the near-field of a conventional emitter used in near-field TPV designs consisting of a thin film of tungsten. The energy density is normalized to that of a black body in the far-field and is calculated using Rytovs fluctuational electrodynamics [6, 66].

The energy density at a distance  $z$  and frequency  $\omega$  is [70]

$$u(z, \omega, T) = \frac{U_{\text{BB}}(\omega, T)}{2} \left\{ \int_0^{k_0} \frac{k_\rho dk_\rho}{k_0 |k_{1z}|} (1 - |r^s|^2) + \frac{(1 - |r^p|^2)}{2} + \int_{k_0}^\infty \frac{k_\rho^3 dk_\rho}{k_0^3 |k_{1z}|} e^{-2\text{Im}(k_{1z})z} (\text{Im}(r^s) + \text{Im}(r^p)) \right\}$$

where  $T$  denotes the temperature.  $k_\rho = \sqrt{k_x^2 + k_y^2}$ ,  $k_0 = \omega/c$ ,  $k_{1z} = \sqrt{k_0^2 - k_\rho^2}$  (such that  $\text{Im}k_{1z} > 0$ ),  $r^s$  and  $r^p$  are the Fresnel reflection coefficients from the thin films for (s) and (p) polarized light respectively and  $\text{Im}$  denotes the imaginary part.  $U_{\text{BB}}(\omega, T)$  is the black body emission spectrum. The near-field energy density enhancement is due to the excitation of weak and lossy surface waves in highly absorptive tungsten (above its plasma wavelength of  $\approx 936$  nm). Due to the lossy nature of tungsten at near-infrared wavelengths [62], the enhancement is low with a broad spectrum. This poor spectral performance is a significant limiting factor for TPVs.

Figure 5(b) shows the near-field energy density near a thin film of GZO. The plasma frequency (ENZ frequency) of the doped zinc-oxide can be tuned to be in the near-infrared spectral range, matched to the bandgap of a TPV cell (GaSb). The spectrally selective nature along with the larger enhancement of near-field energy density, evident in figure 5(b), is due to the excitation of surface plasmons. By controlling the film thickness and ENZ permittivity of the GZO film, the spectral content of near-field enhancement can be tuned to match the high efficiency window of energies directly above the band-gap of a PV cell. For comparison, the thickness of tungsten and GZO are selected such that the peak in energy density enhancement is optimized at the same frequency. The p-TEC outperforms the thin film of tungsten and can be used in both near-field and far-field TPV.

### 5. Thermal topological transitions in graphene multilayers

Thermal emission can also be engineered by controlling the topological transition in a graphene-multilayer structure. A schematic of the graphene multilayers stacked between dielectric slabs of  $\epsilon_d = 2.1$  and thickness  $d = 10$  nm is shown in the inset of figure 6(a). The layers are stacked along the  $z$ -direction. A multilayer structure thus formed has an anisotropic dielectric tensor, whose perpendicular component (along the  $z$ -direction) of the permittivity ( $\epsilon_\perp$ ) is given by the dielectric  $\epsilon_d$ , while the parallel component ( $\epsilon_\parallel$ , parallel to the layers in the  $x$ - $y$  plane) is governed a combination of three factors: (i) the complex conductivity of graphene, (ii) the thickness of the separating substrate ( $d$ ) and (iii) the dielectric  $\epsilon_d$ . The equations for computing the dielectric tensor of the graphene metamaterial are presented in the appendix. Figure 6(a) shows the parallel component (in the  $x$ - $y$  plane) and the perpendicular component (along the  $z$ -direction) of the dielectric tensor when the Fermi energy of each graphene layer is  $E_F = 0.4$  eV. It can be seen that the parallel component of the permittivity changes sign from positive to negative around

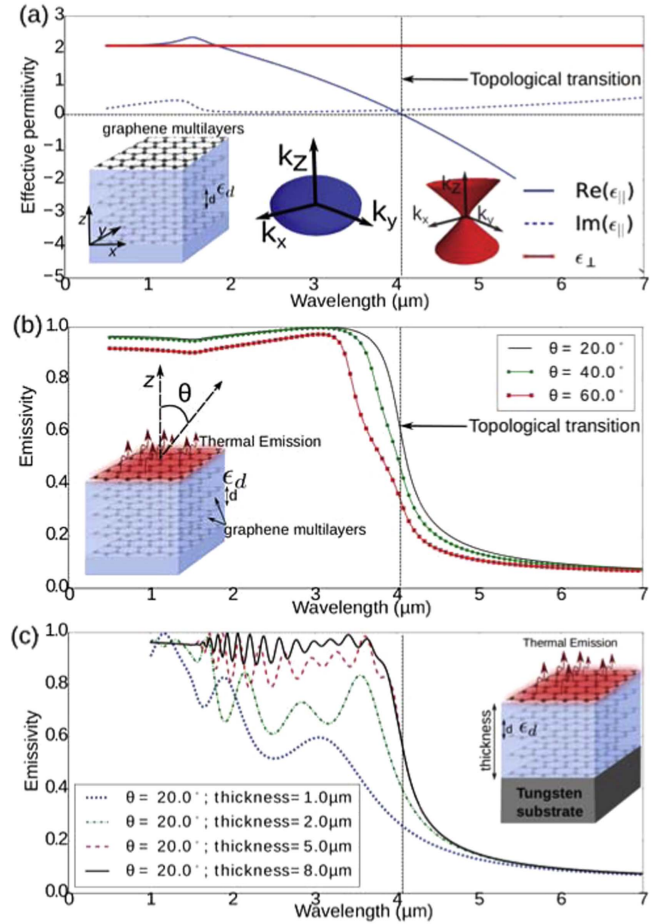


**Figure 6.** Far-field emissivity of a graphene multilayer. (a) The effective permittivity of a graphene multilayer substrate when graphene layers are separated by a dielectric of permittivity 2.1 and a thickness of 10 nm. The Fermi energy of the graphene is  $E_F = 0.4$  eV. The effective permittivity perpendicular to the graphene layers unaffected while the parallel component drops as the excitation wavelength increases. The point where  $\text{Re}(\epsilon_\parallel)$  crosses zero is the topological transition point. (b) The emissivity of the bulk graphene-multilayer at three different angles. (c) The emissivity of varying finite thicknesses of the graphene-multilayer deposited on a tungsten substrate.

4.05  $\mu\text{m}$ , triggering a topological transition from an elliptical to hyperbolic iso-frequency surface, as shown in the inset. At the topological transition wavelength, the emissivity of the structure drops sharply due to a large mismatch in the hyperbolic topology of the graphene-multilayer substrate and the elliptical topology of the free-space. Figure 6(b) shows the suppression of emissivity at different angles from the bulk graphene metamaterial. For thermal emission applications, the graphene metamaterial substrate will need to be deposited on a substrate, such as tungsten. Figure 6(c) shows the emission characteristics of the graphene metamaterial deposited on a tungsten substrate for varying thicknesses of the graphene-multilayer. It can be seen that as the thickness increases beyond 5  $\mu\text{m}$ , its emission characteristics approach those of the bulk graphene. These computations are done for a Fermi-energy of 0.4 eV.

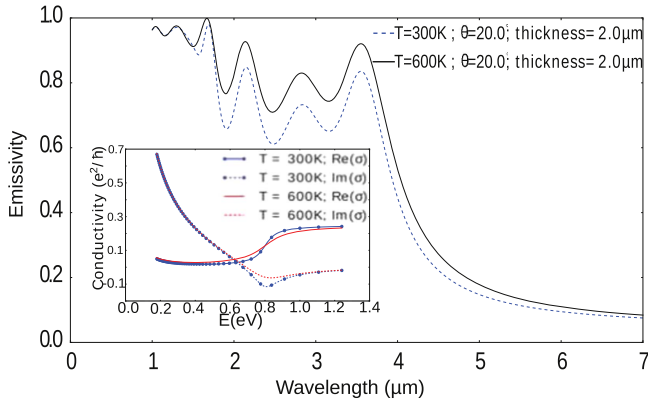


**Figure 7.** Effect of temperature on the far-field emissivity response of the graphene-multilayer structure. The conductivity of the graphene at 300 K and 600 K is shown in the inset.

We would like to point out that the wavelength at which the topological transition in the graphene metamaterial occurs can be controlled by the dielectric thickness  $d$  as well as the Fermi energy of the individual graphene sheets. This gives us an additional degree of freedom in controlling the topological transition wavelength. The graphene metamaterial is also suitable for high temperature applications as its doping concentration and complex conductivity do not vary substantially with temperature [71]. Figure 7 shows the variation in emissivity at temperature  $T = 300$  K and  $T = 600$  K. The change in the complex conductivity of the individual graphene sheets at the two temperatures is shown in the inset. It can be seen that even at a higher temperature, the emissivity of the graphene metamaterial is suppressed at higher wavelengths.

The topological transition in graphene-multilayers also results in enhanced near-field thermal emission. Graphene multilayers support unbounded bulk hyperbolic states which increase the local density of states in vacuum near the surface. This increased local density of states results in enhanced near-field energy density and near-field thermal emission. Figure 8(a) shows the large enhancement in the near-field energy density (normalized to that of a black body), in the hyperbolic region of the spectrum. It can be observed that there is a sharp increase in energy density at the topological transition wavelength. The near-field energy is computed for increasing thicknesses of the graphene-multilayer on a tungsten substrate. It can be seen in the zoomed-in inset that the finite thickness has a small effect on the near-field as compared to the large enhancement triggered by the topological transition. The near-field energy is computed at a distance of 100 nm from the substrate. The topological transition and hence the near-field emission can be tuned by controlling the Fermi energy of the graphene layers. The contour on which the topological transition occurs as a function of the wavelength and Fermi-energy is shown in figure 8(b). The corresponding enhancement in the thermal emission at 600 K is shown in figure 8(c). It is evident that the enhancement in the near-field energy density is triggered at the topological transition for all values of Fermi energy.

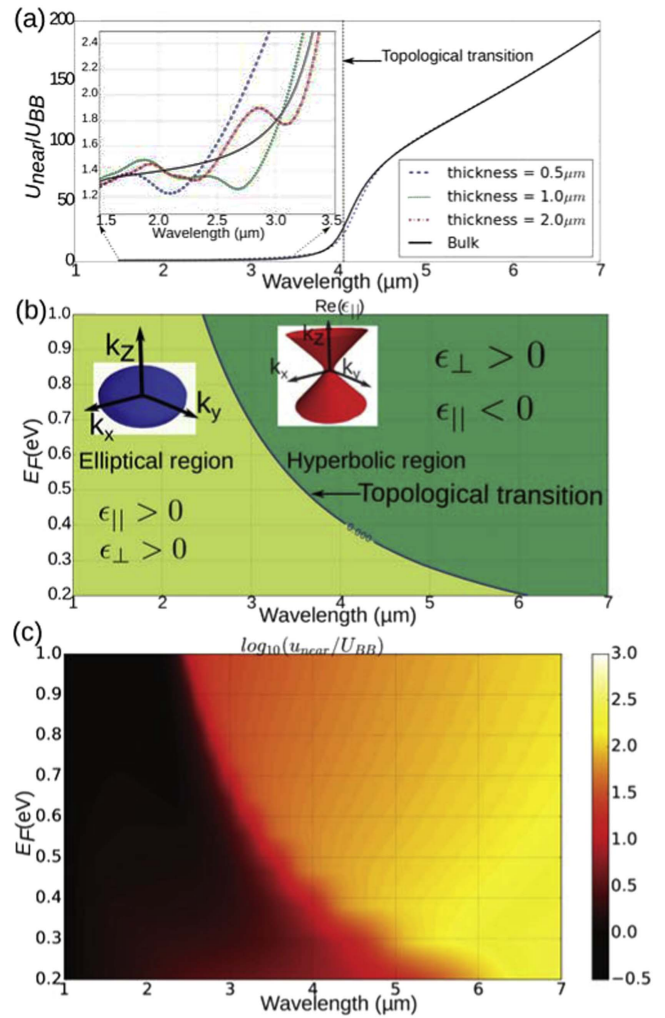


**Figure 8.** (a) Near-field energy density near the graphene-multilayer substrate at a distance of 100 nm above the substrate. The inset shows that the effect of thickness on the energy density is negligible as compared to the enhancement due to bulk topological states. (b) The sign of  $\text{Re}(\epsilon_{||})$  as a function of  $E_F$  and excitation wavelength. A topological transition from an elliptic to hyperbolic substrate occurs on the line  $\text{Re}(\epsilon_{||}) = 0$ . (c) The near-field energy density as a function of  $E_F$  and excitation wavelength. It can be seen that the hyperbolic region of the graphene multilayer enhances the near-surface energy states. The thermal emission is computed at 600 °K.

## 6. Summary

In conclusion, we have introduced the concept of a p-TEC. It functions on the basis of a reflectivity change of metallic thin films near the ENZ frequency. Our approach shows superior performance as compared to Ar coatings and is easier to fabricate than photonic crystals, which require 2D surface patterning of tungsten. We have shown that it achieves narrowband thermal emission in the near-field as compared to tungsten. Developments in high temperature plasmonics can make our thin film design a viable large area technology for thermal emitters. We have also shown that the thermal topological transitions in graphene multilayers can lead to tunable spectrally selective thermal emission.

## Acknowledgments

We acknowledge funding from Alberta Innovates Technology Futures, NSERC, Helmholtz Alberta Initiative and NSF EFRI NEWLAW.

## Appendix A. Thermal emission from the fluctuation dissipation theorem

Any material consists of a large ensemble of fluctuating currents which are the source of thermal radiation. The Poynting vector of the thermal radiation from a material is governed by the fluctuation dissipation theorem. The thermal radiation from a material half-space, in the  $z$ -direction, is given by [70],

$$\langle S_z(\vec{r}, \omega) \rangle = \frac{\omega^2}{4\pi^2 c^2} \frac{\hbar\omega}{e^{\hbar\omega/(K_b T)} - 1} \int_{\Omega=2\pi} A_{\text{emi}} \frac{\cos\theta d\Omega}{2\pi} \quad (\text{A1})$$

where  $\theta$  is the angle from the normal ( $z$ -axis) to the interface, and  $A_{\text{emi}}$  is the emissivity of the material, given by,

$$A_{\text{emi}} = \frac{(1 - |r_{12}^s|^2) + 1 - |r_{12}^p|^2}{2} \quad (\text{A2})$$

where,  $r_{12}^s$  and  $r_{12}^p$  is the reflection coefficient of the  $\hat{s}$  and  $\hat{p}$  polarized wave at the interface of the material and vacuum.

We numerically compute the reflection coefficient at the vacuum/thin-film interface for an  $\hat{s}$  and  $\hat{p}$  polarized wave. These reflection coefficients as a function of frequency and incident angles are then used to compute the far-field and near-field thermal emission.

## Appendix B. Effective permittivity of graphene-multilayers

The complex conductivity of graphene is given by [72, 73],

$$\sigma(\omega, E_F) = \sigma_{\text{intra}} + \sigma_{\text{inter}} \quad (\text{B1})$$

where,

$$\sigma_{\text{intra}} = \frac{2i}{\pi} \left( \frac{K_B T}{(\omega + i\tau^{-1})\hbar} \right) \ln \left( 2 \cosh \left( \frac{E_F}{2TK_B} \right) \right) \quad (\text{B2})$$

and

$$\sigma_{\text{inter}} = \frac{1}{4} \left[ \frac{1}{2} + \frac{1}{\pi} \tan^{-1} \left( \frac{\omega\hbar - 2E_F}{2TK_B} \right) - \frac{i}{2\pi} \ln \left( \frac{\omega\hbar + 2E_F}{(\omega\hbar - 2E_F)^2 + (2TK_B)^2} \right) \right] \quad (\text{B3})$$

where relaxation time  $\tau = 6 \times 10^{-14}$  s,  $T$  is temperature in Kelvin,  $\sigma_{\text{intra}}$  and  $\sigma_{\text{inter}}$  correspond to intra-band and inter-band conductivity, respectively,  $K_B$  is the Boltzmann constant, and  $E_F$  is the Fermi energy.

When the graphene multilayers are stacked between the material of the dielectric constant  $\epsilon_d$  and thickness  $d$  (as shown in the inset of figure 6(a)), the resultant material is

anisotropic, with a dielectric tensor,

$$\leftrightarrow \epsilon = \begin{bmatrix} \epsilon_{\parallel} & 0 & 0 \\ 0 & \epsilon_{\parallel} & 0 \\ 0 & 0 & \epsilon_{\perp} \end{bmatrix} \quad (\text{B4})$$

where  $\epsilon_{\parallel}$  and  $\epsilon_{\perp}$  are the  $x$ - $y$  and  $z$  component of the effective dielectric, respectively [55].

$$\epsilon_{\parallel} = \epsilon_d + \frac{i\sigma(\omega, E_F)}{\omega\epsilon_0 d} \quad (\text{B5})$$

$$\epsilon_{\perp} = \epsilon_d. \quad (\text{B6})$$

For computation of the thermal emission from the graphene metamaterial, the reflection coefficients are computed for the film of the anisotropic dielectric tensor given by equation (B4).

## References

- [1] Bauer T 2011 *Thermophotovoltaics: Basic Principles and Critical Aspects of System Design* (Berlin: Springer)
- [2] Ilic O, Jablan M, Joannopoulos J D, Celanovic I and Soljačić M 2012 Overcoming the black body limit in plasmonic and graphene near-field thermophotovoltaic systems *Opt. Express* **20** A366–84
- [3] Park K, Basu S, King W P and Zhang Z 2008 Performance analysis of near-field thermophotovoltaic devices considering absorption distribution *J. Quant. Spectrosc. Radiat. Transfer* **109** 305–16
- [4] Nefzaoui E, Drevillon J and Joulain K 2012 Selective emitters design and optimization for thermophotovoltaic applications *J. Appl. Phys.* **111** 084316
- [5] Molesky S and Jacob Z 2015 Ideal near-field thermophotovoltaic cells *Phys. Rev. B* **91** 205435
- [6] Zhang Z M 2007 *Nano/Microscale Heat Transfer* (New York: McGraw-Hill)
- [7] Nagasaka Y 2008 *Int. J. Thermophys.* **29** 787–9
- [8] Lin S-Y, Moreno J and Fleming J G 2003 Three-dimensional photonic-crystal emitter for thermal photovoltaic power generation *Appl. Phys. Lett.* **82** 380–2
- [9] Yeng Y X, Ghebrehirhan M, Bermel P, Chan W R, Joannopoulos J D, Soljačić M and Celanovic I 2012 Enabling high-temperature nanophotonics for energy applications *Proc. Natl Acad. Sci.* **109** 2280–5
- [10] Guler U, Boltasseva A and Shalaev V M 2014 Refractory plasmonics *Science* **344** 263–4
- [11] Molesky S, Dewalt C J and Jacob Z 2013 High temperature epsilon-near-zero and epsilon-near-pole metamaterial emitters for thermophotovoltaics *Opt. Express* **21** A96–110
- [12] Guo Y, Molesky S, Hu H, Cortes C L and Jacob Z 2014 Thermal excitation of plasmons for near-field thermophotovoltaics *Appl. Phys. Lett.* **105** 073903
- [13] Nagpal P, Han S E, Stein A and Norris D J 2008 Efficient low-temperature thermophotovoltaic emitters from metallic photonic crystals *Nano Lett.* **8** 3238–43
- [14] Rephaeli E and Fan S 2009 Absorber and emitter for solar thermo-photovoltaic systems to achieve efficiency exceeding the shockley-queisser limit *Opt. Express* **17** 15145–59
- [15] Narayanaswamy A and Chen G 2005 Thermal radiation in 1D photonic crystals *J. Quant. Spectrosc. Radiat. Transfer* **93** 175–83
- [16] Celanovic I, O'Sullivan F, Jovanovic N, Qi M and Kassakian J G 2004 1D and 2D photonic crystals for thermophotovoltaic applications *Proc. SPIE* **5450** 416

- [16] Wang Z, Luk T S, Tan Y, Ji D, Zhou M, Gan Q and Yu Z 2015 Tunneling-enabled spectrally selective thermal emitter based on flat metallic films *Appl. Phys. Lett.* **106** 101104
- [17] Song B et al 2015 Enhancement of near-field radiative heat transfer using polar dielectric thin films *Nat. Nanotechnol.* **10** 253–8
- [18] Basu S and Francoeur M 2011 Maximum near-field radiative heat transfer between thin films *Appl. Phys. Lett.* **98** 243120
- [19] Edalatpour S and Francoeur M 2013 Size effect on the emissivity of thin films *J. Quant. Spectrosc. Radiat. Transfer* **118** 75–85
- [20] DiMatteo R S, Greiff P, Finberg S L, Young-Waithe K A, Choy H, Masaki M M and Fonstad C G 2001 Enhanced photogeneration of carriers in a semiconductor via coupling across a nonisothermal nanoscale vacuum gap *Appl. Phys. Lett.* **79** 1894–6
- [21] Narayanaswamy A and Chen G 2003 Surface modes for near field thermophotovoltaics *Appl. Phys. Lett.* **82** 3544–6
- [22] Joulain K and Henkel C 2008 The near field correlation spectrum of a metallic film *Appl. Phys. B* **93** 151–8
- [23] Nefedov I S and Simovski C R 2011 Giant radiation heat transfer through micron gaps *Phys. Rev. B* **84** 195459
- [24] Tong J K, Hsu W-C, Huang Y, Boriskina S V and Chen G 2015 Thin-film thermal well emitters and absorbers for high-efficiency thermophotovoltaics *Sci. Rep.* **5** 10661
- [25] Dyachenko P, Molesky S, Petrov A Y, Störmer M, Krekeler T, Lang S, Ritter M, Jacob Z and Eich M 2016 Controlling thermal emission with refractory epsilon-near-zero metamaterials via topological transitions, *Nat. Commun.* **7** 11809
- [26] Mason J, Smith S and Wasserman D 2011 Strong absorption and selective thermal emission from a midinfrared metamaterial *Appl. Phys. Lett.* **98** 241105
- [27] Liu X, Tyler T, Starr T, Starr A F, Jokerst N M and Padilla W J 2011 Taming the blackbody with infrared metamaterials as selective thermal emitters *Phys. Rev. Lett.* **107** 045901
- [28] Wu C, Neuner B III, John J, Milder A, Zollars B, Savoy S and Shvets G 2012 Metamaterial-based integrated plasmonic absorber/emitter for solar thermo-photovoltaic systems *J. Opt.* **14** 024005
- [29] Zhao B, Wang L, Shuai Y and Zhang Z M 2013 Thermophotovoltaic emitters based on a two-dimensional grating/thin-film nanostructure *Int. J. Heat Mass Transfer* **67** 637–45
- [30] Neuner B III, Wu C, ten Eyck G, Sinclair M, Brener I and Shvets G 2013 Efficient infrared thermal emitters based on low-albedo polaritonic meta-surfaces *Appl. Phys. Lett.* **102** 211111
- [31] Messina R and Ben-Abdallah P 2012 Graphene-based photovoltaic cells for near-field thermal energy conversion *Sci. Rep.* **3** 1383
- [32] Svetovoy V and Palasantzas G 2014 Graphene-on-silicon near-field thermophotovoltaic cell *Phys. Rev. Appl.* **2** 034006
- [33] Ben-Abdallah P, Marquier F and Greffet J-J 2013 Controlling thermal radiation with surface waves *Plasmonics: Theory and Applications* (Dordrecht: Springer) pp 283–327
- [34] Joulain K, Mulet J-P, Marquier F, Carminati R and Greffet J-J 2005 Surface electromagnetic waves thermally excited: Radiative heat transfer, coherence properties and casimir forces revisited in the near field *Surf. Sci. Rep.* **57** 59–112
- [35] Deng H, Li Z, Stan L, Rosenmann D, Czaplewski D, Gao J and Yang X 2015 Broadband perfect absorber based on one ultrathin layer of refractory metal *Opt. Lett.* **40** 2592–5
- [36] Drevillon J, Joulain K, Ben-Abdallah P and Nefzaoui E 2011 Far field coherent thermal emission from a bilayer structure *J. Appl. Phys.* **109** 034315
- [37] Lee B and Zhang Z 2007 Coherent thermal emission from modified periodic multilayer structures *J. Heat Transfer* **129** 17–26
- [38] Wang L, Lee B, Wang X and Zhang Z 2009 Spatial and temporal coherence of thermal radiation in asymmetric fabry-perot resonance cavities *Int. J. Heat Mass Transfer* **52** 3024–31
- [39] Brar V W, Sherrott M C, Jang M S, Kim S, Kim L, Choi M, Sweatlock L A and Atwater H A 2015 Electronic modulation of infrared radiation in graphene plasmonic resonators *Nat. Commun.* **6** 7032
- [40] van Zwol P, Joulain K, Abdallah P B, Greffet J-J and Chevrier J 2011 Fast nanoscale heat-flux modulation with phase-change materials *Phys. Rev. B* **83** 201404
- [41] Fang Z, Wang Y, Schlather A E, Liu Z, Ajayan P M, Garcia de Abajo F J, Nordlander P, Zhu X and Halas N J 2013 Active tunable absorption enhancement with graphene nanodisk arrays *Nano Lett.* **14** 299–304
- [42] Freitag M, Chiu H-Y, Steiner M, Perebeinos V and Avouris P 2010 Thermal infrared emission from biased graphene *Nat. Nanotechnol.* **5** 497–501
- [43] Thongrattanasiri S, Koppens F H and de Abajo F J G 2012 Complete optical absorption in periodically patterned graphene *Phys. Rev. Lett.* **108** 047401
- [44] Bolotin K I, Sikes K, Jiang Z, Klima M, Fudenberg G, Hone J, Kim P and Stormer H 2008 Ultrahigh electron mobility in suspended graphene *Solid State Commun.* **146** 351–5
- [45] Ghosh S, Calizo I, Teweldebrhan D, Pokatilov E, Nika D, Balandin A, Bao W, Miao F and Lau C N 2008 Extremely high thermal conductivity of graphene: Prospects for thermal management applications in nanoelectronic circuits *Appl. Phys. Lett.* **92** 151911
- [46] Koppens F H, Chang D E and Garcia de Abajo F J 2011 Graphene plasmonics: a platform for strong light-matter interactions *Nano Lett.* **11** 3370–7
- [47] Pu M, Chen P, Wang Y, Zhao Z, Wang C, Huang C, Hu C and Luo X 2013 Strong enhancement of light absorption and highly directive thermal emission in graphene *Opt. Express* **21** 11618–27
- [48] Ilic O, Jablan M, Joannopoulos J D, Celanovic I, Buljan H and Soljačić M 2012 Near-field thermal radiation transfer controlled by plasmons in graphene *Phys. Rev. B* **85** 155422
- [49] Lim M, Lee S S and Lee B J 2013 Near-field thermal radiation between graphene-covered doped silicon plates *Opt. Express* **21** 22173–85
- [50] Iorsh I V, Mukhin I S, Shadrivov I V, Belov P A and Kivshar Y S 2013 Hyperbolic metamaterials based on multilayer graphene structures *Phys. Rev. B* **87** 075416
- [51] Zhang L, Zhang Z, Kang C, Cheng B, Chen L, Yang X, Wang J, Li W and Wang B 2014 Tunable bulk polaritons of graphene-based hyperbolic metamaterials *Opt. Express* **22** 14022–30
- [52] Sreekanth K, de Luca A and Strangi G 2013 Negative refraction in graphene-based hyperbolic metamaterials *Appl. Phys. Lett.* **103** 023107
- [53] Othman M A, Guclu C and Capolino F 2013 Graphene-based tunable hyperbolic metamaterials and enhanced near-field absorption *Opt. Express* **21** 7614–32
- [54] Linder J and Halterman K 2016 Graphene-based extremely wide-angle tunable metamaterial absorber *Sci. Rep.* **6** 31225
- [55] Chang Y-C, Liu C-H, Liu C-H, Zhang S, Marder S R, Narimanov E E, Zhong Z and Norris T B 2016 Realization of mid-infrared graphene hyperbolic metamaterials, *Nat. Commun.* **7** 10568
- [56] Lenert A, Bierman D M, Nam Y, Chan W R, Celanović I, Soljačić M and Wang E N 2014 A nanophotonic solar thermophotovoltaic device *Nat. Nanotechnol.* **9** 126–30
- [57] Li W, Guler U, Kinsey N, Naik G V, Boltasseva A, Guan J, Shalaev V M and Kildishev A V 2014 Refractory plasmonics with titanium nitride: broadband metamaterial absorber *Adv. Mater.* **26** 7959–65

- [58] Pradhan A, Mundle R, Santiago K, Skuza J, Xiao B, Song K, Bahoura M, Cheaito R and Hopkins P E 2014 Extreme tunability in aluminum doped zinc oxide plasmonic materials for near-infrared applications *Sci. Rep.* **4** 6415
- [59] Kim J, Naik G V, Gavrilenko A V, Dondapati K, Gavrilenko V I, Prokes S, Glembocki O J, Shalaev V M and Boltasseva A 2013 Optical properties of gallium-doped zinc oxide—a low-loss plasmonic material: first-principles theory and experiment *Phys. Rev. X* **3** 041037
- [60] Krishnamoorthy H N, Jacob Z, Narimanov E, Kretzschmar I and Menon V M 2012 Topological transitions in metamaterials *Science* **336** 205–9
- [61] Naik G V, Kim J and Boltasseva A 2011 Oxides and nitrides as alternative plasmonic materials in the optical range [invited] *Opt. Mater. Express* **1** 1090–9
- [62] Roberts S 1959 Optical properties of nickel and tungsten and their interpretation according to drude's formula *Phys. Rev.* **114** 104
- [63] Costescu R M, Wall M A and Cahill D G 2003 Thermal conductance of epitaxial interfaces *Phys. Rev. B* **67** 054302
- [64] Schmid P E, Sunaga M S and Lévy F 1998 Optical and electronic properties of sputtered tin thin films *J. Vac. Sci. Technol. A* **16** 2870–5
- [65] Larruquert J I, Pérez-Marín A P, García-Cortés S, Rodríguez-de Marcos L, Aznárez J A and Méndez J A 2012 Self-consistent optical constants of sputter-deposited b 4 c thin films *J. Opt. Soc. Am. A* **29** 117–23
- [66] Liu X, Zhao B and Zhang Z M 2015 Enhanced near-field thermal radiation and reduced casimir stiction between doped-si gratings *Phys. Rev. A* **91** 062510
- [67] Greffet J-J and Nieto-Vesperinas M 1998 Field theory for generalized bidirectional reflectivity: derivation of helmholtz reciprocity principle and Kirchhoff's law *J. Opt. Soc. Am. A* **15** 2735–44
- [68] Fraas L M, Samaras J E and Avery J E 2001 Antireflection coated refractory metal matched emitters for use in thermophotovoltaic generators *US Patent Specification* US6271461
- [69] Basu S and Zhang Z 2009 Maximum energy transfer in near-field thermal radiation at nanometer distances *J. Appl. Phys.* **105** 093535
- [70] Joulain K 2007 Radiative transfer on short length scales *Microscale and Nanoscale Heat Transfer* (Berlin: Springer) pp 107–31
- [71] Fang X-Y, Yu X-X, Zheng H-M, Jin H-B, Wang L and Cao M-S 2015 Temperature- and thickness-dependent electrical conductivity of few-layer graphene and graphene nanosheets *Phys. Lett. A* **379** 2245–51
- [72] Wunsch B, Stauber T, Sols F and Guinea F 2006 Dynamical polarization of graphene at finite doping *New J. Phys.* **8** 318
- [73] Hwang E and Sarma S D 2007 Dielectric function, screening, and plasmons in two-dimensional graphene *Phys. Rev. B* **75** 205418